

Microwave Microscope Studies of Trapped Vortex Dynamics in Superconductors

Chung-Yang Wang¹ and Steven M. Anlage¹

¹*Quantum Materials Center, Department of Physics,
University of Maryland, College Park, Maryland 20742, USA*

Trapped vortices in superconductors introduce residual resistance in superconducting radio-frequency (SRF) cavities and disrupt the operation of superconducting quantum and digital electronic circuits. Understanding the detailed dynamics of trapped vortices under oscillating magnetic fields is essential for advancing these technologies. We have developed a near-field magnetic microwave microscope to study the dynamics of a limited number of trapped vortices under the probe when stimulated by a localized rf magnetic field. By measuring the local second-harmonic response (P_{2f}) at sub-femto-Watt levels, we isolate signals exclusively arising from trapped vortices, excluding contributions from surface defects and Meissner screening currents. Toy models of Niobium superconductor hosting vortex pinning sites are introduced and studied with Time-Dependent Ginzburg-Landau (TDGL) simulations of probe/sample interaction to better understand the measured second-harmonic response. The simulation results demonstrate that the second-harmonic response of trapped vortex motion under a localized rf magnetic field shares key features with the experimental data. This measurement technique provides access to vortex dynamics at the micron scale, such as depinning events and spatially-resolved pinning properties, as demonstrated in measurements on a Niobium film with an antidot flux pinning array.

I. INTRODUCTION

Stray magnetic vortices that become pinned in superconductors contribute to enhanced losses in superconducting radio-frequency (SRF) cavities and corrupt the operation of superconducting electronics. In SRF cavities, trapped vortices introduce residual resistance, limiting the achievable quality factor [1–15]. For superconducting quantum circuits, trapped vortices add loss [16–18], which serve to limit the coherence time of superconducting qubits operating at microwave frequencies. On the other hand, trapped vortices at current-nodes of a superconducting resonator can also be used to capture non-equilibrium quasiparticles and relax them [19]. For superconducting digital circuits, pinned vortices not only degrade performance but, in extreme cases, can compromise circuit functionality entirely [20–29]. The effects of trapped vortices in superconducting digital circuits are usually thought of in terms of DC bias currents that the vortices add to the circuits. However, in this work we investigate an effect that has largely been overlooked in the context of superconducting digital circuits, namely the microwave frequency response of trapped vortices in superconductors.

The behavior of trapped vortices under stimulation by an oscillating magnetic field [30] is often studied macroscopically, focusing on the average properties of many trapped vortices, such as loss, critical current density, and pinning energy [31–38]. These measurements are generally interpreted in terms of collective single-coordinate models (e.g., Gittleman-Rosenblum type models) [39–44], which subsumes the response of individual vortices to the rf currents. While these models provide insights into the average properties of all trapped vortices in a sample, direct high-frequency microscopic measurements at the level of individual trapped vortices remain challenging. Furthermore, beyond measur-

ing loss, it is essential to understand the detailed dynamics of trapped vortices under oscillating magnetic fields. To achieve this, we need to study small numbers of vortices pinned in superconductors to understand their full dynamics and pinning properties.

Here we introduce a near-field magnetic microwave microscope approach [45–58] to study the dynamics of a limited number of trapped vortices under the probe (at micron length scales) by stimulating them with a localized and intense rf magnetic field and analyzing the second-harmonic response (P_{2f}) generated by their resulting motion.

Various microscopic techniques have been employed to study individual vortices in superconductors, including magnetic force microscopy (MFM) [59], scanning superconducting quantum interference device (SQUID) [60, 61], single-vortex confinement structures [62], scanning Hall probe microscopy [63], and scanning tunneling microscopy (STM) [64]. These methods have provided invaluable insights into vortex behavior. However, they do not directly probe the microwave response of vortices. In contrast, our approach employs a near-field magnetic microwave microscope to investigate the high-frequency response of trapped vortices, enabling the study of their dynamics under localized microwave excitation.

The response of a superconductor to an oscillating magnetic field can be classified by symmetry into odd harmonic responses (linear response, third-harmonic response, etc.) and even harmonic responses (second-harmonic response, fourth-harmonic response, etc.), which probe fundamentally different aspects of superconducting dynamics [65–74]. Odd harmonic responses [45, 47–55, 75] capture contributions from a variety of mechanisms, including Meissner screening currents [76, 77], nonlinearities from current-dependent superfluid density variation, and rf vortex nucleation [56, 57]. In contrast, even harmonic responses [37, 47–49] are known

to vanish in the absence of time reversal invariance breaking [65, 67–69], such as when no DC magnetic field is applied and no vortices are trapped in the superconductor. Notably, in the absence of an external offset (field or current), the second-harmonic response collects signals from trapped vortices exclusively, effectively filtering out contributions from other mechanisms. This exclusivity makes P_{2f} a powerful tool for studying trapped vortices [37].

In previous research, we demonstrated that our microwave microscope can study surface defects that nucleate rf vortices by measuring the *third*-harmonic response P_{3f} [57]. These rf vortices are nucleated and destroyed twice in each rf cycle [3, 78]. In this work, we show that the same microwave microscope can be used to instead study trapped DC vortices by measuring the *second*-harmonic response, P_{2f} .

However, the second-harmonic response has some subtleties associated with its interpretation. We show that the magnitude of the second-harmonic response is *not* directly proportional to the density of trapped vortices, or the surface impedance of the sample. Note that it is not our goal to measure the critical current density or the vortex depinning frequency (which is an effective macroscopic property of many vortices) associated with trapped DC vortices. Instead, P_{2f} is sensitive to a limited number of vortices and their detailed configuration and dynamics beneath the probe of our microwave microscope, and hence can be used to detect *changes in* trapped vortex configuration.

In this work, we experimentally study a Nb film with an antidot vortex pinning array. Our results suggest that this measurement technique is useful for detecting depinning events of trapped vortices at the micron scale and studying spatially-resolved pinning properties.

The structure of this paper is as follows: Sec. II describes the experimental setup. In Sec. III, we discuss the mechanism underlying the second-harmonic response observed in our measurements and use Time-Dependent Ginzburg-Landau (TDGL) simulations to highlight three key features of the second-harmonic response associated with trapped vortex dynamics. Sec. IV presents the experimental results obtained from the Nb film. Finally, in Sec. V, we summarize our findings and discuss the capabilities of this measurement technique.

II. EXPERIMENTAL SETUP

Near-field microwave microscopy of materials properties [79–95] has also proven to be very helpful in the study of superconducting microwave devices [96–99]. The setup of our near-field magnetic microwave microscope is identical to that described in Ref. [57, 58]. A brief overview of the microscope is provided in this section.

The core component of our microwave microscope is a magnetic writer head (provided by Seagate Technology), commonly used in conventional hard-disk drives. This

magnetic writer head can generate a localized rf magnetic field. In our setup, a Seagate magnetic writer head is mounted on a cryogenic XYZ positioner and operated in a scanning probe microscope configuration.

The microwave source (HP 83620B) signal $P_{rf}\sin^2(\omega t)$ is sent to the probe (magnetic writer head) via its built-in transmission line. The probe then produces a localized rf magnetic field $B_{rf}\sin(\omega t)$ acting on the sample surface. Trapped vortices in the sample then wiggle and generate a response magnetic field that is coupled back to the same probe, creating a propagating signal whose second-harmonic component $P_{2f}\sin^2(2\omega t)$ is then extracted and measured by a spectrum analyzer (Aaronia RSA250X) at room temperature. In practice, a complicated multi-harmonic signal comes back to room temperature, but we filter out just the second-harmonic response.

With magnetic shielding in place, the residual DC magnetic field near the sample at low temperatures is found to be approximately $2.1 \mu\text{T}$, as measured with an in-situ cryogenic 3-axis magnetometer (Bartington Cryomag-100).

The spatial resolution of the microscope ranges from sub-micron to micron scale, depending on the probe-sample separation, and the signal being analyzed. The spatial resolution for measurements of second-harmonic response is estimated to be approximately $1.1 \mu\text{m}$ for this specific setup (see Appendix A).

III. NUMERICAL SIMULATIONS

The dynamics of trapped vortices under stimulation by a localized rf magnetic field is a complex topic. A comprehensive numerical investigation is beyond the scope of this work. Instead, this section aims to illustrate key features of P_{2f} associated with trapped vortex dynamics using numerical simulations of simplified toy models (Niobium superconductor hosting vortex pinning sites). These insights will later be used to analyze the experimental results (Sec. IV).

In the following, we first introduce our simulation framework (Sec. III A), then discuss the mechanism underlying the second-harmonic response observed in our measurements (Sec. III B), and finally present three core features using various toy models (Sec. III C, Sec. III D, and Sec. III E).

A. Introduction to numerical simulations

The Time-Dependent Ginzburg-Landau (TDGL) model is a widely used framework for studying vortex dynamics in superconductors [14, 36, 100–107]. In previous work, we employed TDGL simulations to investigate rf vortex nucleation and P_{3f} [56, 57, 78]. In this work, we use the same simulation framework to study trapped vortex dynamics and P_{2f} . In the following, we provide a brief overview of the key settings used in the TDGL

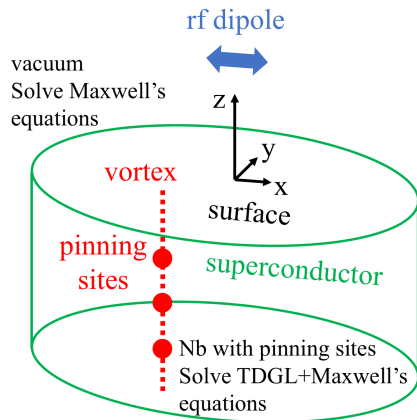


FIG. 1. A schematic representation of the TDGL simulations and toy models. The blue double arrow represents the rf dipole, the red dots represent the pinning sites, and the red dashed line represents the trapped vortex.

simulations, as the detailed descriptions are provided in Ref. [57]. The equations, boundary conditions, material parameters, and the setting of toy models of the TDGL simulations can be found in Appendix B.

Figure 1 provides a schematic representation of the TDGL simulations and toy models. In our measurements, the applied field generated by the microwave microscope probe is a localized rf magnetic field with a configuration similar to that produced by a point dipole aligned parallel to the sample surface. In the simulations, the probe is approximated as a pointlike magnetic dipole located at $(x_{dp}, y_{dp}, h_{dp}) = (0, 0, 400 \text{ nm})$, oriented in the x-direction, and having a sinusoidal time-dependent magnetic moment $(M_{dp}\sin(\omega t), 0, 0)$ with a frequency of $\omega/2\pi=1.7 \text{ GHz}$. To quantify the strength of the rf magnetic field, the peak rf magnetic field amplitude experienced by the superconductor is specified and is denoted as B_{pk} .

Note that the TDGL simulations are fully three-dimensional, hence quite demanding in terms of memory usage and processing time. The model is inhomogeneous in the sense that it consists of both a vacuum region, which hosts the rf dipole acting as a source of high frequency magnetic field, and a superconducting region which hosts the DC vortex (see Fig. 1). Maxwell's equations are solved in the vacuum region, while the coupled TDGL equations, along with Maxwell's equations are solved inside the superconductor, and appropriate boundary conditions are enforced at the surfaces.

The simulation domain is of finite size, and no periodic boundary conditions are imposed. Since the primary vortex dynamics occur near the origin, the influence of finite-size effects is mitigated by selecting a sufficiently large simulation domain and applying appropriate boundary conditions. Further details are provided in Appendix B.

The primary addition to the setup described in Ref. [57] is the inclusion of single-flux-quantum trapped mag-

netic vortices. To generate trapped vortices, spherical pinning sites composed of a low- T_c impurity phase are introduced into the Nb domain, and a uniform DC magnetic field is applied along the z-direction. DC vortices aligned in the z-direction then nucleate at the boundary of the superconducting domain and propagate inward, spreading throughout the superconducting region. While most of these vortices remain unpinned and free to move, some become pinned at the pinning sites. Once these vortices are pinned, the external DC magnetic field is subsequently *removed*. The unpinned vortices repel each other and eventually exit the simulation domain, leaving only the pinned vortices localized at the pinning sites.

After the unpinned vortices have left the simulation domain, the rf magnetic field is applied for five rf cycles, and P_{2f} at the location of the dipole is calculated based on the vortex dynamics observed during the fifth rf cycle.

B. Origin of second-harmonic response

Consider a system driven by a sinusoidal driving force with angular frequency ω . Let the response function be denoted as $f(t)$. The even components of the Fourier transform of $f(t)$ vanish if $f(t) = -f(t + \pi/\omega)$, meaning the response function exhibits perfect symmetry between the two half-cycles. In other words, even harmonic responses quantify the asymmetric component between the two half-cycles of $f(t)$. As the leading-order term of even harmonic responses, the second-harmonic response is frequently analyzed in such studies.

In the context of this work, the system consists of trapped vortices in superconductors, and the driving force is an oscillating magnetic field created by a scanned dipole over the surface of the superconductor. When trapped vortices are stimulated by an oscillating magnetic field, they wiggle in response, and the asymmetric component of this motion generates even harmonic responses.

The asymmetry in time of trapped vortex dynamics can arise from various mechanisms. One such mechanism involves an asymmetric potential experienced by vortices, which may originate intrinsically in noncentrosymmetric superconductors [108, 109], be introduced through artificially engineered asymmetric potentials [110–113], or be created by the combination of a symmetric pinning potential and a DC current acting as a bias [37, 111]. In our case, the asymmetry originates from the localized and inhomogeneous nature of the rf magnetic field generated by the microwave microscope. This rf magnetic field induces a screening current, which in turn generates a Lorentz force acting on trapped vortices [39, 40, 43, 44]. Due to the strong spatial gradient of the rf magnetic field, both the screening current and the resulting Lorentz force exhibit significant spatial gradients. During an rf cycle, a trapped vortex experiences a stronger Lorentz force when moving toward regions of higher magnetic field strength and a weaker force when moving away, resulting in asym-

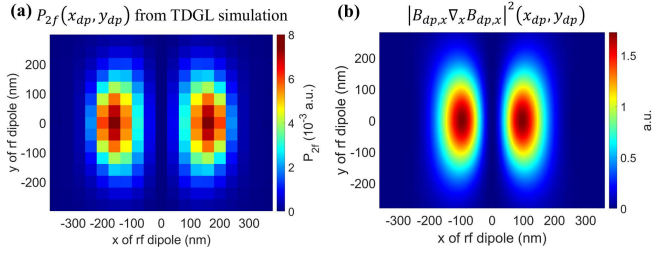


FIG. 2. Asymmetry in time of the dynamics of a trapped vortex (at $(x, y) = (0, 0)$) as a function of dipole location (x_{dp}, y_{dp}) , for $h_{dp} = 400$ nm. (a) TDGL simulation results of P_{2f} as a function of dipole location (x_{dp}, y_{dp}) for toy model 1 (a vortex pinned at $(x, y) = (0, 0)$), at $T = 7.44$ K and $B_{pk} = 28.3$ mT. (b) The plot of $|B_{dp,x} \nabla_x B_{dp,x}|^2$ at $(x, y) = (0, 0)$ as a function of dipole location (x_{dp}, y_{dp}) , where $B_{dp,x}$ is the x-component of the magnetic field at the surface of a superconductor created by a magnetic dipole.

metric vortex dynamics between the two half-cycles.

It is informative to ask: For a vortex pinned at $(x, y) = (0, 0)$, how does its dynamics vary as a function of the dipole location (x_{dp}, y_{dp}) with fixed height h_{dp} ? Figure 2(a) shows the TDGL simulation results for P_{2f} (recovered at the location of the dipole) as a function of (x_{dp}, y_{dp}) , for a vortex pinned at $(x, y) = (0, 0)$ (toy model 1). It essentially represents the second-harmonic point-spread function of a single trapped DC vortex, as imaged by our near-field magnetic microwave microscope. The pattern of $P_{2f}(x, y)$ shown in Fig. 2(a) can be understood as follows.

The Lorentz force F_{Lorentz} acting on a trapped vortex is proportional to the local current density J , which, to first-order approximation, is proportional to the magnitude of the magnetic field B_{total} . At the superconductor surface ($z = 0$), $B_{\text{total}} = 2B_{\text{external}}$ by considering the image method and the boundary condition that the perpendicular component of the magnetic field must vanish at $z = 0$. In other words, at $z = 0$, we have

$$F_{\text{Lorentz}} \propto J \propto B_{\text{total}} = 2B_{\text{external}}. \quad (1)$$

In our case, B_{external} is the external magnetic field at $z = 0$ created by the rf dipole.

Since the rf dipole is oriented in the x-direction, the induced current is primarily in the y-direction, creating a Lorentz force on the vortex in the x-direction, and the motion of the trapped vortex is predominantly along the x-axis. Roughly speaking, the asymmetry in the vortex motion is proportional to both the strength of the Lorentz force exerted on the vortex by J_y and its spatial gradient at $z = 0$. Consequently, an estimate of P_{2f} at the surface of the superconductor is given by

$$P_{2f}(x_{dp}, y_{dp}) \propto |J_y \nabla_x J_y|^2 \propto |B_{dp,x} \nabla_x B_{dp,x}|^2, \quad (2)$$

where $B_{dp,x}$ is the x-component of the dipole magnetic field (B_{external} in this case) at $z = 0$. The analytic expressions for $B_{dp,x}$ and $B_{dp,x} \nabla_x B_{dp,x}$ due to a magnetic

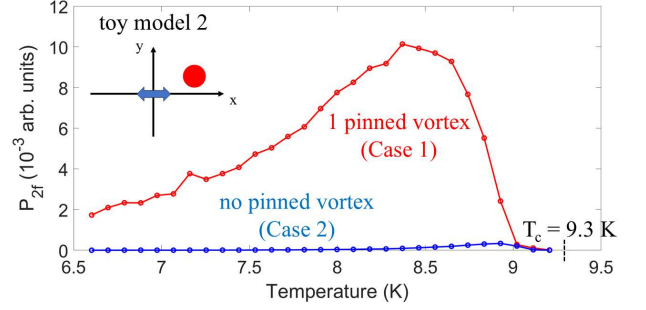


FIG. 3. TDGL simulation results of $P_{2f}(T)$ ($B_{pk} = 28.3$ mT) for toy model 2 under two scenarios. There is one pinned vortex for the red curve (Case 1) and there is no pinned vortex for the blue curve (Case 2). The inset shows the top-view setup of toy model 2: The blue double arrows represent the rf dipole, and the red dot represents the vortex (Case 1) pinned by pinning sites.

dipole above the surface of a superconductor are provided in Appendix C.

Figure 2(b) presents $|B_{dp,x} \nabla_x B_{dp,x}|^2$ experienced at $(x, y) = (0, 0)$ as a function of scanned dipole location (x_{dp}, y_{dp}) . The strong similarity between Fig. 2(a) and Fig. 2(b) supports the qualitative validity of Eq. 2. A key feature shared by both figures is that the asymmetry vanishes along the entire y-axis ($x_{dp} = 0$). In Fig. 2(b), this occurs because $\nabla_x B_{dp,x} = 0$. In Fig. 2(a), the system exhibits symmetry between the $-x$ and $+x$ directions, leading to symmetric vortex dynamics between the two half-cycles, which results in $P_{2f} = 0$. Note that $P_{2f} = 0$ when the dipole is positioned directly above the trapped vortex ($(x_{dp}, y_{dp}) = (0, 0)$) even though there is a significant Lorentz force acting on the vortex. Figure 2(a) clearly demonstrates that P_{2f} reflects the asymmetry of the vortex dynamics rather than simply indicating the presence of a trapped vortex right beneath the dipole. In the case of multiple trapped vortices, P_{2f} remains a measure of the asymmetry in their collective dynamics rather than being proportional to their number.

It is worth pointing out that the pinning potential in toy model 1 enjoys rotational symmetry about the z-axis. The asymmetry in the wiggling motion of the trapped vortex (except along the y-axis) originates from the strong gradient of the localized rf magnetic field itself at the vortex location rather than from any intrinsic asymmetry in the pinning potential. Consequently, this technique, measuring P_{2f} with our microwave microscope, remains effective even for trapped vortices in symmetric pinning potentials.

For the rest of the simulations (toy models 2 to 6), the dipole is fixed at $(x_{dp}, y_{dp}, h_{dp}) = (0, 0, 400$ nm).

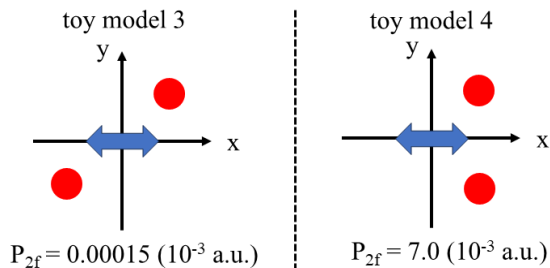


FIG. 4. TDGL simulation results of P_{2f} for toy models 3 and 4, at $T = 7.44$ K and $B_{pk} = 28.3$ mT. The top-view shows a projection of the rf dipole (blue arrows) and the red dots represent vortices pinned by pinning sites.

C. Trapped vortices and P_{2f}

Core Feature 1: P_{2f} arises exclusively in the presence of trapped vortices and is absent when no trapped vortices are present.

Figure 3 shows $P_{2f}(T)$ for toy model 2 under two scenarios. In Case 1 (red curve), a single pinned vortex is present, while in Case 2 (blue curve), no pinned vortex is present. Both cases use identical conditions and pinning potentials, with the only difference being the presence or absence of a trapped vortex at the pinning sites. In Case 1, the wiggling of the trapped vortex generates P_{2f} . In Case 2, there is no trapped vortex, and hence $P_{2f} = 0$. The slight bump observed in the blue curve around 8.8 K is attributed to numerical errors (slight asymmetries in the computed response between the two half-cycles).

D. Trapped vortex configuration and P_{2f}

Core Feature 2: P_{2f} is highly sensitive to the specific configuration of trapped vortices.

Figure 4 shows P_{2f} for toy models 3 and 4, both of which contain two trapped vortices. Despite this similarity, the values of P_{2f} differ dramatically. In fact, P_{2f} is expected to be zero for toy model 3, as the vortex dynamics is perfectly symmetric by design; the small nonzero value observed in simulations (noted on the Figure) arises from numerical errors. This comparison between toy models 3 and 4 highlights that P_{2f} can vary significantly with changes in the trapped vortex configuration. Since P_{2f} reflects the time-asymmetry in vortex dynamics, it is inherently sensitive to the detailed arrangement of trapped vortices.

E. Changes in trapped vortex configuration

Core Feature 3: Changes in the trapped vortex configuration can cause abrupt jumps in $P_{2f}(T)$.

One manifestation of Core Feature 2 is that vortex configuration changes as the temperature increases, which

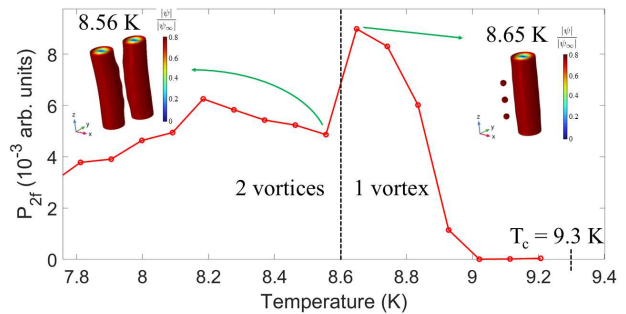


FIG. 5. TDGL simulation results for $P_{2f}(T)$ for toy model 5 at $B_{pk} = 28.3$ mT. The two insets display the normalized order parameter (ψ/ψ_∞) at $T=8.56$ K and $T=8.65$ K, providing a visualization of the trapped vortices and pinning sites (red spheres).

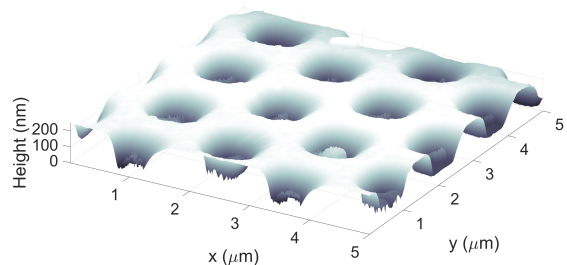


FIG. 6. An atomic force microscopy (AFM) image of a $5 \times 5 \mu\text{m}^2$ surface area of the Nb antidot film sample.

can result in a jump (up or down) in $P_{2f}(T)$. Figure 5 shows $P_{2f}(T)$ for toy model 5. At low temperatures ($T < 8.6$ K), two vortices remain pinned. As the temperature increases beyond 8.6 K, one of the pinned vortices becomes depinned and escapes from the simulation due to the vortex-vortex repulsive force exceeding the pinning force provided by the pinning sites. This depinning event causes a dramatic jump in $P_{2f}(T)$ around 8.6 K, as shown in Fig. 5.

Since P_{2f} reflects the time-asymmetry in vortex dynamics rather than being proportional to the number of trapped vortices, its value can either increase or decrease when a pinned vortex is removed. An example of $P_{2f}(T)$ exhibiting a downward jump upon vortex depinning is provided in Appendix D.

IV. EXPERIMENTAL RESULTS

A. Sample information

Antidot arrays in superconducting films serve as engineered traps for vortices [32–35, 63, 111–115]. In this work, we study a 170-nm-thick Nb film with an antidot flux pinning array on a SiOx substrate. The antidot array has a period of $1.6 \mu\text{m}$ and an antidot diameter of $1.2 \mu\text{m}$.

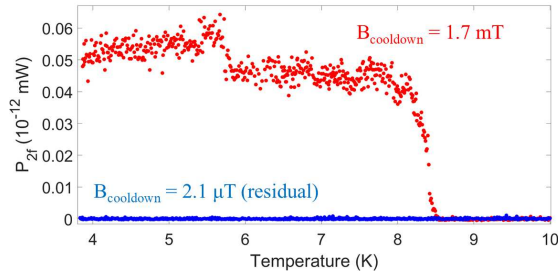


FIG. 7. Representative data for P_{2f} as a function of temperature during a warmup measurement for two different cooldown fields. The red dots are the data for $B_{\text{cooldown}} = 1.7$ mT and the blue dots are the data for $B_{\text{cooldown}} = 2.1$ μ T. The input frequency is 1.81 GHz, and the input power is 6.8 dBm.

Figure 6 shows an atomic force microscopy (AFM) image of a 5×5 μm^2 surface area of the sample. Note that the substrate is exposed in the antidot regions of the film.

B. Measurement protocol

A representative measurement protocol is as follows. Initially, the probe (magnetic writer head) is positioned away from the sample. To create trapped vortices, the sample is first warmed to 10 K, well above the transition temperature. A DC magnetic field (B_{cooldown}) is then applied, and then the sample is gradually cooled from 10 K (above T_c) to 6.5 K (below T_c) at a rate of 0.55 mK/s. The sample is subsequently cooled rapidly from 6.5 K to 3.8 K (base temperature). Once the temperature stabilizes at 3.8 K, the DC magnetic field is *removed*. The probe is then brought into contact with the sample by adjusting the piezo stages. The microwave source is then activated with a fixed input frequency f and power, and P_{2f} is measured as the sample is gradually warmed from 3.8 K to 10 K. During this warmup process, the surface of the sample is exposed to a fixed rf magnetic field, $B_{\text{RF}}\sin(\omega t)$, over a micron-scale area. Notably, *no* DC magnetic field is applied during the microwave measurements, ensuring that the measured P_{2f} originates solely from trapped vortices in the sample.

The magnetic writer head itself exhibits temperature-independent nonlinearity. Since the measured P_{2f} is a combination of the probe background and the sample contribution, the probe background, determined by averaging the magnitude of $P_{2f}(T)$ between 9.5 K and 10 K, is subtracted from the total signal to isolate the sample response. See Appendix E for further details about the background subtraction process.

C. Representative data of $P_{2f}(T)$

Figure 7 shows the representative data for the linear power scale $P_{2f}(T)$ during a warmup measurement at a fixed location on the sample, for two different cooldown fields. The input frequency is $f = \omega/2\pi = 1.81$ GHz, and the input power is +6.8 dBm (at the room temperature microwave source).

The red dots are the data for $B_{\text{cooldown}} = 1.7$ mT. This cooldown magnetic field corresponds to an average flux quanta separation ($\sqrt{\Phi_0/B_{\text{cooldown}}}$) of 1.11 μm , a filling fraction of the antidot lattice of 1.70, and an average of 8.3 flux quanta in the field of view of the microwave microscope probe (see Appendix A). The $P_{2f}(T)$ shows a clear transition around 8.6 K, which is the T_c of the sample. For $T < 8.6$ K, vortices are trapped in the sample, and their wiggling under stimulation by the rf magnetic field generates P_{2f} . For $T > 8.6$ K, the sample loses superconductivity and the trapped vortices are released, and hence P_{2f} vanishes.

The blue dots are the data for $B_{\text{cooldown}} = 2.1$ μ T, which is the measured residual DC magnetic field when no external field is applied. This cooldown magnetic field corresponds to an average flux quanta separation of 31.40 μm , a filling fraction of the antidot lattice of 0.0021, and an average of 0.01 flux quanta in the field of view of the microwave microscope probe. Because the density of trapped vortices is very low, with high probability, there are no trapped vortices in the field of view of the probe, and thus there is no P_{2f} .

The contrast between the two data sets (red and blue) in Fig. 7 clearly demonstrates that P_{2f} originates from vortices trapped in the sample that are in the field of view of the probe, which agrees with Core Feature 1 (see Sec. III C).

For simplicity, in the following text, the term “trapped vortices” will refer specifically to those within the field of view of the microwave microscope probe.

A distinct discrete jump in $P_{2f}(T)$ is observed around 5.75 K for $B_{\text{cooldown}} = 1.7$ mT in Fig. 7. In the following, the temperature of such a discrete jump is denoted as $T_{P_{2f}(T)\text{jump}}$. One possible explanation for this $P_{2f}(T)$ jump is as follows: For temperatures slightly below 5.75 K, the trapped vortices are arranged in a specific configuration. As the temperature increases to approximately 5.75 K, the configuration of the trapped vortices changes. This change in configuration leads to the discrete jump in $P_{2f}(T)$ (see Sec. III E), since the measured P_{2f} comes from the superposition of the contributions of all the trapped vortices under the probe. The interpretation of $P_{2f}(T)$ jumps as indicators of vortex configuration changes is supported by the observation of P_{2f} hysteresis in temperature sweeps (see Appendix F).

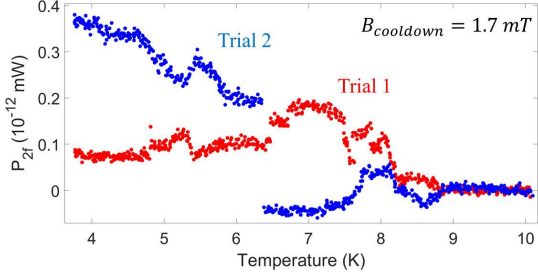


FIG. 8. Two repeated measurements of $P_{2f}(T)$ at nominally the same location of the Nb film sample for $B_{\text{cooldown}} = 1.7$ mT. The input frequency is 1.819 GHz, and the input power is -5 dBm.

D. Statistics of $P_{2f}(T)$ jumps

The measured value of P_{2f} is highly sensitive to the details of trapped vortex configurations (see Sec. III D), which are complex and inherently stochastic. For example, Fig. 8 presents two repeated measurements of $P_{2f}(T)$ performed at the same location under nominally identical conditions, where the contrast between Trial 1 (red) and Trial 2 (blue) highlights this stochastic behavior. (A discussion on the negative $P_{2f}(T)$ observed in Trial 2 is provided in Appendix E.) Given this sensitivity, rather than focusing on the absolute value of P_{2f} , we analyze $P_{2f}(T)$ jumps, which serve as indicators of changes in trapped vortex configurations and are therefore closely related to pinning properties.

To further investigate $P_{2f}(T)$ jumps, we perform repeated measurements of $P_{2f}(T)$ from 3.8 K to above T_c at nominally the same location of the Nb film sample and analyze the statistical properties of $T_{P_{2f}(T)\text{jump}}$.

Figure 9(a) presents the statistical distribution of $T_{P_{2f}(T)\text{jump}}$ as a function of temperature. The data is obtained from 10 repeated measurements of $P_{2f}(T)$ during a temperature sweep from 3.8 K to above T_c , conducted nominally at the same location on the sample surface, with $B_{\text{cooldown}} = 0.64$ mT. This cooldown magnetic field corresponds to an average flux quanta separation of $1.80 \mu\text{m}$, a filling fraction of the antidot lattice of 0.65, and an average of 3.2 flux quanta in the field of view of the microwave microscope probe.

The distribution in Fig. 9(a) reveals three distinct clusters: one above $T_{P_{2f}(T)\text{jump}}/T_c = 0.8$, another peaked around $T_{P_{2f}(T)\text{jump}}/T_c = 0.72$, and a third below $T_{P_{2f}(T)\text{jump}}/T_c = 0.6$.

The rearrangement of trapped vortices as the temperature increases is inherently complex, potentially resulting in a multi-component $T_{P_{2f}(T)\text{jump}}$ distribution. For example, an Abrikosov vortex might jump from one pinning site to a nearby pinning site [64, 116], be attracted to and captured by an antidot, or flux trapped by antidots could rearrange into other antidots near T_c .

The three distinct clusters in Fig. 9(a) suggest the presence of three different types of trapped vortex rear-

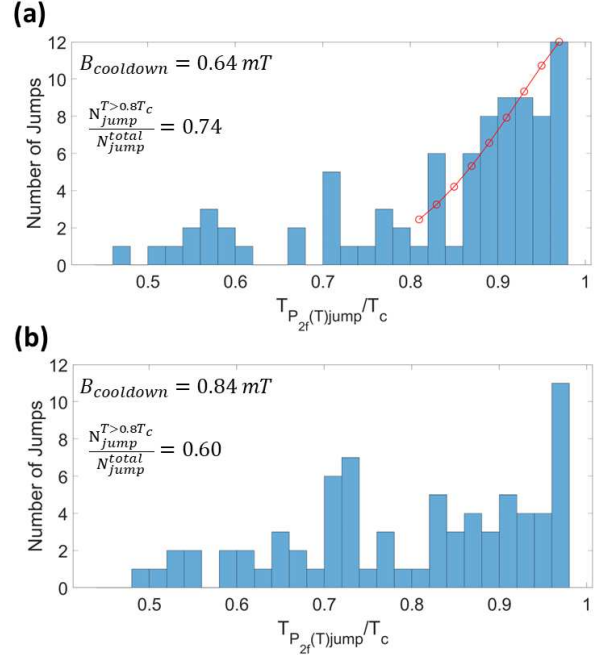


FIG. 9. Histogram of the temperatures at which $P_{2f}(T)$ jumps occur ($T_{P_{2f}(T)\text{jump}}$). The data is obtained from 10 repeated measurements of $P_{2f}(T)$ from 3.8 K to above T_c at Location 1. Panels (a) and (b) correspond to cooldown fields of $B_{\text{cooldown}} = 0.64$ mT and $B_{\text{cooldown}} = 0.84$ mT, respectively. The input frequency is 1.708 GHz, and the input power is -3 dBm. The red curve in panel (a) is the fitting result using Eqs. 3 and 4.

angement events in the sample. The profiles and temperatures of these clusters provide insight into the pinning properties of the sample. Notably, the cluster above $T_{P_{2f}(T)\text{jump}}/T_c = 0.8$ accounts for more than half of the total $P_{2f}(T)$ jumps. Specifically, the high-temperature jump ratio, defined as $N_{\text{jump}}^{T > 0.8T_c} / N_{\text{jump}}^{\text{total}}$, is 0.74 for Fig. 9(a).

One possible mechanism for trapped vortex rearrangement events is thermal activation [40, 43, 44, 116–119]. Under this mechanism, trapped vortices are expected to rearrange more frequently at higher temperatures, consistent with the trend observed in the cluster above $T_{P_{2f}(T)\text{jump}}/T_c = 0.8$ in Fig. 9(a). To analyze the data further, assume a temperature-dependent activation energy $U(T)$ as [119–126]

$$U(T) = U_0 \left(1 - \frac{T}{T_c} \right)^\gamma \quad (3)$$

where γ is a scaling exponent. Assume the likelihood of trapped vortex rearrangement events $P(T)$ due to thermal activation at temperature T is given by

$$P(T) \propto e^{-\frac{U(T)}{k_B T}}. \quad (4)$$

Assuming that trapped vortex rearrangement events for $T > 0.8 T_c$ in Fig. 9(a) are primarily driven by thermal

Location	U_0 (meV)	γ	$U(T)$ (meV) for $0.30 < T/T_c < 0.48$
1	10.97	1.43	between 4.26 and 6.57
2	9.86	1.76	between 3.08 and 5.25

TABLE I. Summary of the vortex pinning parameters (U_0 and γ) extracted from $P_{2f}(T)$ measurements using Eqs. 3 and 4. Data are presented for two distinct locations on the sample surface (Location 1 and Location 2), separated by $50 \mu\text{m}$.

activation, with vortex-vortex interactions playing a minor role, we fit the probability distribution above $T = 0.8 T_c$ using Eqs. 3 and 4. The resulting fit yields a pinning potential of $U_0 = 14.8 k_B T_c = 127.3 \text{ K} = 10.97 \text{ meV}$ and a scaling exponent of $\gamma = 1.43$.

Building on this analysis, we investigate the spatially-resolved vortex pinning properties (U_0 and γ) of the sample. We perform measurements following the same procedure as described in Fig. 9(a) (Location 1) but at a different location on the sample surface (Location 2). Locations 1 and 2 are separated by $50 \mu\text{m}$. The extracted pinning parameters for these two locations are summarized in Table I.

Several previous studies have described the temperature dependence of the activation energy $U(T)$ using the form given by Eq. 3. Typically, the exponent γ falls within the range $0.5 < \gamma < 2$ [123–125]. In our analysis, we obtained $\gamma = 1.43$ and 1.76 at Locations 1 and 2, respectively, which are consistent with values commonly reported in the literature.

Vortex pinning properties in Nb films have previously been studied in Ref. [119], where a temperature-independent activation energy of 1.9 meV was obtained by fitting experimental data in the temperature range $0.3 < T/T_c < 0.48$. In contrast, we use a temperature-dependent activation energy $U(T)$ described by Eq. 3; our fitted values in the same temperature range, summarized in the last column of Table I, are comparable to that reported in Ref. [119]. Furthermore, our results also agree in magnitude with the activation energies of Pb-Tl alloy, reported to be between 3 meV and 14 meV in Ref. [117].

Taken together, these comparisons confirm that the pinning parameters (U_0 and γ) obtained from our analysis are consistent with values reported in the literature, thus validating the physical reasonability of our results.

Figure 9(b) shows the statistical distribution of $T_{P_{2f}(T)\text{jump}}$ as a function of temperature for $B_{\text{cooldown}} = 0.84 \text{ mT}$. The measurement procedure is identical to that of Fig. 9(a), except with a higher B_{cooldown} , resulting in an increased trapped vortex density. Compared to Fig. 9(a) ($N_{\text{jump}}^{T>0.8T_c}/N_{\text{jump}}^{\text{total}} = 0.74$), the distribution of $T_{P_{2f}(T)\text{jump}}$ in Fig. 9(b) is more spread out, with a lower high-temperature jump ratio of $N_{\text{jump}}^{T>0.8T_c}/N_{\text{jump}}^{\text{total}} = 0.60$.

Building on the results from Fig. 9, we extend the measurements to multiple B_{cooldown} values, corresponding to different trapped vortex densities, at four distinct loca-

Cooldown from room temperature to 3.8 K	Location	input frequency (GHz)	input power (dBm)
First	1	1.708	-3
	2		
Second	3	1.819	-5
	4		

TABLE II. Summary of the measurement details at four distinct locations on the sample surface. Locations 1 and 2 are separated by $50 \mu\text{m}$, as are Locations 3 and 4. Measurements at Locations 1 and 2 were performed during the same cooldown from room temperature to 3.8 K , while measurements at Locations 3 and 4 were obtained in a separate cooldown from room temperature to 3.8 K .

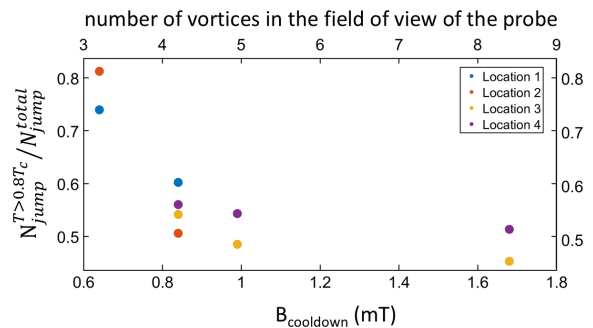


FIG. 10. High-temperature jump ratio $N_{\text{jump}}^{T>0.8T_c}/N_{\text{jump}}^{\text{total}}$ for different B_{cooldown} values, measured at four distinct locations on the sample surface. The measurement details at the four locations are summarized in Table II. The data in Fig. 9 is obtained at Location 1.

tions on the sample surface (Locations 1 to 4). The measurement details at the four locations are summarized in Table II. Figure 10 presents the high-temperature jump ratio $N_{\text{jump}}^{T>0.8T_c}/N_{\text{jump}}^{\text{total}}$ as a function of B_{cooldown} .

As shown in Fig. 10, $N_{\text{jump}}^{T>0.8T_c}/N_{\text{jump}}^{\text{total}}$ decreases with increasing B_{cooldown} across all four measurement locations. One possible explanation for this trend is as follows. In the low trapped vortex density regime (small B_{cooldown}), vortex-vortex interactions are weak, and trapped vortex rearrangement events are primarily driven by thermal activation, which is most significant near T_c . In contrast, in the high trapped vortex density regime (large B_{cooldown}), the trapped vortex configuration becomes more complex, as both the pinning potential of the antidot array and vortex-vortex interactions play a significant role. In this regime, trapped vortices can rearrange even at lower temperatures.

Understanding trapped vortex rearrangement mechanisms beyond thermal activation near T_c requires more sophisticated theoretical analysis and numerical simulations, which are beyond the scope of this work.

V. CONCLUSION

In this work, we present a proof-of-principle study demonstrating the use of local P_{2f} measurements with our near-field magnetic microwave microscope to investigate the dynamics of trapped vortices at the micron scale. This microscopic approach complements traditional methods that average the behavior of many vortices. Specifically, we show that this technique can reveal depinning events and provide insights into spatially-resolved pinning properties. Furthermore, our results highlight how vortex pinning behavior varies across different trapped vortex density regimes, offering a new perspective on the interplay between pinning potentials and vortex-vortex interactions. It is particularly relevant for applications such as SRF cavities, superconducting quantum circuits, and superconducting digital electronics. Future work includes developing more sophisticated models beyond the thermal activation mechanism to further extract quantitative information about pinning properties from P_{2f} measurements.

VI. ACKNOWLEDGEMENT

We would like to thank Javier Guzman from Seagate Technology for providing magnetic write heads, and Cougar Garcia for assistance. We also thank Thomas Antonsen for helpful discussions. This work is supported by DOE/HEP under grant DESC0017931, and by ARO/FSDL under grant ARO W911NF-24-1-0153.

Appendix A: Field of view of the near-field microwave probe

The field of view of the probe can be estimated using a Monte Carlo approach. For instance, if the average number of trapped vortices within the field of view of the probe for a given B_{cooldown} value is 0.4, the probability of the probe interacting with a trapped vortex and detecting the P_{2f} signal is 40%. In practice, we perform 6 repeated measurements of $P_{2f}(T)$ (with an input frequency of 1.824 GHz and input power of 6 dBm) and record how many trials exhibit a transition near the T_c of the sample in the low trapped vortex density regime (small B_{cooldown} values). For $B_{\text{cooldown}} = 0.061$ mT, 0.124 mT, and 0.188 mT, the number of trials showing a sample signal out of 6 are 2, 4, and 5, respectively. Based on these results, the interaction range between the probe and trapped vortices is estimated to be approximately 1.1 μm .

Appendix B: Equations and parameters for TDGL simulations

The two TDGL equations solved in this work are [127, 128]

$$\gamma \frac{\partial \psi}{\partial t} = \frac{-1}{2m_*} (-i\hbar\nabla - e_*A)^2 \psi - \alpha\psi - \beta |\psi|^2 \psi \quad (\text{B1})$$

and

$$\begin{aligned} \sigma \frac{\partial A}{\partial t} = & \frac{-i\hbar e_*}{2m_*} (\psi^* \nabla \psi - \psi \nabla \psi^*) - \frac{e_*^2}{m_*} |\psi|^2 A \\ & - \frac{1}{\mu_0} \nabla \times \nabla \times A. \end{aligned} \quad (\text{B2})$$

Here $e_* = 2e$ is the charge of the Cooper pair, $m_* = 2m_e$ is the mass of the Cooper pair, $\gamma = \frac{\pi\hbar|\alpha|}{8k_B(T_c-T)}$ plays the role of a friction coefficient, ψ is the order parameter, A is the total vector potential (arising from both external and self-generated sources), σ is the electric conductivity of the normal state, and both α and β are material-specific phenomenological parameters. Note that α and β can be related to the penetration depth λ and the thermodynamic critical field B_c by

$$\lambda = \sqrt{\frac{m_*\beta}{\mu_0 e_*^2 |\alpha|}} \quad (\text{B3})$$

and

$$B_c = \frac{\sqrt{\mu_0} |\alpha|}{\sqrt{\beta}}. \quad (\text{B4})$$

The total current is the combination of the supercurrent J_s and the normal current J_n . The supercurrent J_s is given by

$$J_s = \frac{-i\hbar e_*}{2m_*} (\psi^* \nabla \psi - \psi \nabla \psi^*) - \frac{e_*^2}{m_*} |\psi|^2 A \quad (\text{B5})$$

and the normal current J_n is given by

$$J_n = \sigma E = -\sigma \frac{\partial A}{\partial t}. \quad (\text{B6})$$

For boundary conditions, any current passing through the boundary between a superconductor and a vacuum is unphysical. Therefore, the boundary conditions must be enforced along the entire enclosing boundary $\partial\Omega$ of the superconducting simulation domain, including the sides and bottom surfaces. Specifically, we expect:

$$\nabla\psi \cdot \hat{n} = 0 \quad \text{on} \quad \partial\Omega. \quad (\text{B7})$$

$$A \cdot \hat{n} = 0 \quad \text{on} \quad \partial\Omega. \quad (\text{B8})$$

Here \hat{n} is the unit vector normal to the boundary.

In the toy models studied in this work (Niobium superconductor hosting vortex pinning sites), a pinning site is modeled as a spherical region of radius r_{pin} composed of a low- T_c impurity phase. Pinning sites are incorporated

toy model	x_{pin} (nm)	y_{pin} (nm)	r_{pin} (nm)
1	0	0	40
2	120	80	40
3	80	80	40
4	80	80	40
5	120	80	40
6	120	80	40
	120	-80	18

TABLE III. Summary of the pinning site configurations for toy models 1 to 6. All toy models include either one or two sets of pinning sites, with each set consisting of three identical pinning sites sharing the same $(x_{\text{pin}}, y_{\text{pin}})$ coordinates. The z_{pin} values for the three sites are -200 nm, -360 nm, and -520 nm. See Appendix D for the discussion of toy model 6.

by introducing spatial variations in five material-specific parameters: T_c , α , β , γ , and σ . The values of α and β are determined for a given choice of λ and B_c using Eqs. B3 and B4. For simplicity, the normal state conductivity σ of the low- T_c impurity phase is set to be the same as that of Nb. The critical temperature, penetration depth, and critical field of Nb are 9.3 K, 40 nm, and 200 mT, respectively. For the low- T_c impurity phase, these values are 3.0 K, 90 nm, and 120 mT, respectively.

The location of a pinning site is represented by $(x_{\text{pin}}, y_{\text{pin}}, z_{\text{pin}})$, where $z_{\text{pin}} < 0$ since the sample occupies the $z < 0$ region. All toy models include either one or two sets of pinning sites, with each set consisting of three identical pinning sites sharing the same $(x_{\text{pin}}, y_{\text{pin}})$ coordinates. The z_{pin} values for the three sites are -200 nm, -360 nm, and -520 nm. Each set of pinning sites can then be labeled by its x_{pin} , y_{pin} , and r_{pin} . The pinning site configurations are summarized in Table III.

Appendix C: Magnetic field of a point dipole

Here we present the magnetic field generated by a point dipole in free space at the xy-plane ($z = 0$). Consider a pointlike magnetic dipole located at $(x_{\text{dp}}, y_{\text{dp}}, h_{\text{dp}})$, oriented in the x-direction, with a magnetic moment M . The x-component of the dipole magnetic field at $(x, y, z = 0)$ is given by

$$B_{\text{dp},x}(x, y) = \frac{\mu_0 M}{4\pi} \frac{3(x - x_{\text{dp}})^2 - r^2}{r^5}, \quad (\text{C1})$$

where $r = \sqrt{(x - x_{\text{dp}})^2 + (y - y_{\text{dp}})^2 + h_{\text{dp}}^2}$. For $B_{\text{dp},x} \nabla_x B_{\text{dp},x}$, we have

$$B_{\text{dp},x} \nabla_x B_{\text{dp},x} = \left(\frac{\mu_0 M}{4\pi} \right)^2 \frac{3(x - x_{\text{dp}})^2 - r^2}{r^{12}} \times 3(x - x_{\text{dp}}) [3r^2 - 5(x - x_{\text{dp}})^2]. \quad (\text{C2})$$

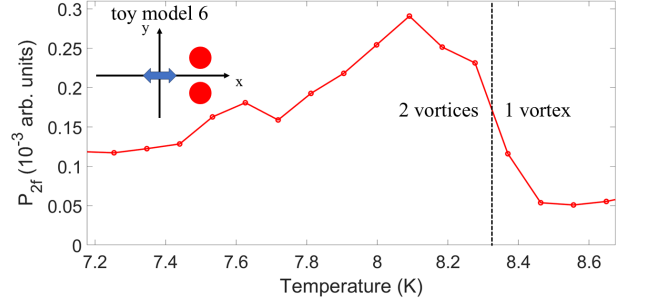


FIG. 11. TDGL simulation results for $P_{2f}(T)$ for toy model 6 at $B_{\text{pk}} = 5.7$ mT. The blue double arrow represents the rf dipole, and the red dots represent vortices pinned by pinning sites.

Appendix D: Another simulated $P_{2f}(T)$ for two pinned vortices

Here we provide another example of simulated $P_{2f}(T)$. Figure 11 shows $P_{2f}(T)$ for toy model 6. The setting of pinning sites configuration of toy model 6 is described in Table III. At low temperatures ($T < 8.32$ K), two vortices remain pinned. As the temperature increases beyond 8.32 K, one of the pinned vortices becomes depinned and escapes from the simulation due to the vortex-vortex repulsive force exceeding the pinning force provided by the pinning sites. This depinning event causes a noticeable downward jump in $P_{2f}(T)$ around 8.32 K, as shown in Fig. 11.

Appendix E: Subtraction of probe background

Since the measured P_{2f} is the superposition of the probe background and the sample signal, the total measured signal may be weaker than the probe background if these two components are out of phase [50]. In the absence of phase information, we perform a simple scalar subtraction of the probe background from the total signal. This naive background subtraction can result in negative P_{2f} values.

Appendix F: Hysteresis in P_{2f} in temperature sweeps

Figure 12 shows a 3-stage zigzag temperature sweep measurement of P_{2f} . The sample is first cooled from 10 K to 6.5 K with $B_{\text{cooldown}} = 1.7$ mT. The DC magnetic field is then removed, and three successive microwave measurements are performed: stage 1 involves warming from 6.5 K to 8.3 K (red), stage 2 involves cooling back from 8.3 K to 6.5 K (green), and stage 3 involves a second warming from 6.5 K to 8.3 K (blue). Note that the sample remains below T_c in this entire P_{2f} measurement process. In stage 1, three discrete jumps in $P_{2f}(T)$ are

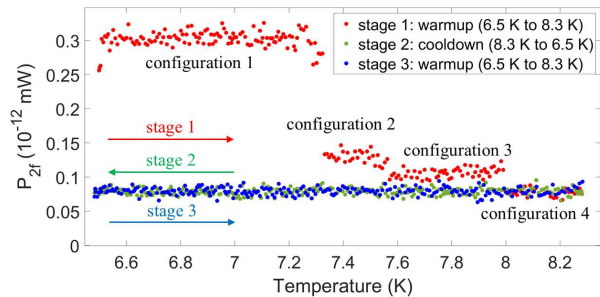


FIG. 12. A 3-stage zigzag temperature sweep measurement of P_{2f} at a fixed location on the sample surface. The input frequency is 1.818 GHz, and the input power is 2 dBm.

observed, whereas $P_{2f}(T)$ remains nearly temperature-independent during stages 2 and 3. This 3-stage zigzag temperature sweep clearly demonstrates the hysteresis of P_{2f} when $P_{2f}(T)$ jumps are present.

One possible interpretation is as follows: At the beginning of stage 1, the vortex configuration is metastable. As

the temperature increases, the trapped vortices rearrange themselves into progressively more stable configurations (from configuration 1 to configuration 4), which is reflected in the $P_{2f}(T)$ jumps. Configuration 4 is the most stable among the four configurations, and thus the vortices tend to remain in this configuration during stages 2 and 3. This hysteresis behavior of $P_{2f}(T)$ jumps aligns with the hypothesis that these jumps correspond to transitions of trapped vortices from less stable to more stable configurations.

As additional evidence of the hysteresis behavior of P_{2f} , Fig. 13 presents spatially-scanned images of P_{2f} at multiple temperatures. The sample is first cooled from 10 K to 7 K with $B_{\text{cooldown}} = 1.7$ mT. The DC magnetic field is then removed, and three successive microwave measurements are performed: the first image at 7 K (left), the second image after warming from 7 K to 8.2 K $< T_c$ (center), and the third image after cooling back from 8.2 K to 7 K (right). The contrast between the left and right images clearly demonstrates the hysteresis behavior of P_{2f} .

-
- [1] C. Benvenuti, S. Calatroni, I.E. Campisi, P. Dariulat, M.A. Peck, R. Russo, and A.-M. Valente, “Study of the surface resistance of superconducting niobium films at 1.5 GHz,” *Physica C: Superconductivity* **316**, 153–188 (1999).
- [2] G. Ciovati and A. Gurevich, “Evidence of high-field radio-frequency hot spots due to trapped vortices in niobium cavities,” *Phys. Rev. ST Accel. Beams* **11**, 122001 (2008).
- [3] A. Gurevich and G. Ciovati, “Dynamics of vortex penetration, jumpwise instabilities, and nonlinear surface resistance of type-II superconductors in strong rf fields,” *Phys. Rev. B* **77**, 104501 (2008).
- [4] S. Aull, O. Kugeler, and J. Knobloch, “Trapped magnetic flux in superconducting niobium samples,” *Phys. Rev. ST Accel. Beams* **15**, 062001 (2012).
- [5] A. Gurevich and G. Ciovati, “Effect of vortex hotspots on the radio-frequency surface resistance of superconductors,” *Phys. Rev. B* **87**, 054502 (2013).
- [6] A. Romanenko, A. Grassellino, A. C. Crawford, D. A. Sergatskov, and O. Melnychuk, “Ultra-high quality factors in superconducting niobium cavities in ambient magnetic fields up to 190 mG,” *Applied Physics Letters* **105**, 234103 (2014).
- [7] A. Romanenko, A. Grassellino, O. Melnychuk, and D. A. Sergatskov, “Dependence of the residual surface resistance of superconducting radio frequency cavities on the cooling dynamics around T_c ,” *Journal of Applied Physics* **115**, 184903 (2014).
- [8] Dan Gonnella, John Kaufman, and Matthias Liepe, “Impact of nitrogen doping of niobium superconducting cavities on the sensitivity of surface resistance to trapped magnetic flux,” *Journal of Applied Physics* **119**, 073904 (2016).
- [9] S. Posen, M. Checchin, A. C. Crawford, A. Grassellino, M. Martinello, O. S. Melnychuk, A. Romanenko, D. A. Sergatskov, and Y. Trenikhina, “Efficient expulsion of magnetic flux in superconducting radiofrequency cavities for high Q applications,” *Journal of Applied Physics* **119**, 213903 (2016).
- [10] Pashupati Dhakal and Gianluigi Ciovati, “Effect of cooldown and residual magnetic field on the performance of niobium-copper clad superconducting radio-frequency cavity,” *Superconductor Science and Technology* **31**, 015006 (2017).
- [11] Hasan Padamsee, “50 years of success for SRF accelerators—a review,” *Superconductor science and technology* **30**, 053003 (2017).
- [12] M Checchin, M Martinello, A Grassellino, A Romanenko, and J F Zasadzinski, “Electron mean free path dependence of the vortex surface impedance,” *Superconductor Science and Technology* **30**, 034003 (2017).
- [13] Danilo B. Liarte, Daniel Hall, Peter N. Koufalis, Akira Miyazaki, Alen Senanian, Matthias Liepe, and James P. Sethna, “Vortex dynamics and losses due to pinning: Dissipation from trapped magnetic flux in resonant superconducting radio-frequency cavities,” *Phys. Rev. Appl.* **10**, 054057 (2018).
- [14] Jared Carlson, Alden Pack, Mark K. Transtrum, Jaeyel Lee, David N. Seidman, Danilo B. Liarte, Nathan S. Sitaraman, Alen Senanian, Michelle M. Kelley, James P. Sethna, *et al.*, “Analysis of magnetic vortex dissipation in Sn-segregated boundaries in Nb3Sn superconducting RF cavities,” *Physical Review B* **103**, 024516 (2021).
- [15] B D Khanal, S Balachandran, S Chetri, M Barron, R Mullinix, A Williams, P Xu, A Ingle, P J Lee, G Ciovati, and P Dhakal, “Role of microstructure on flux expulsion

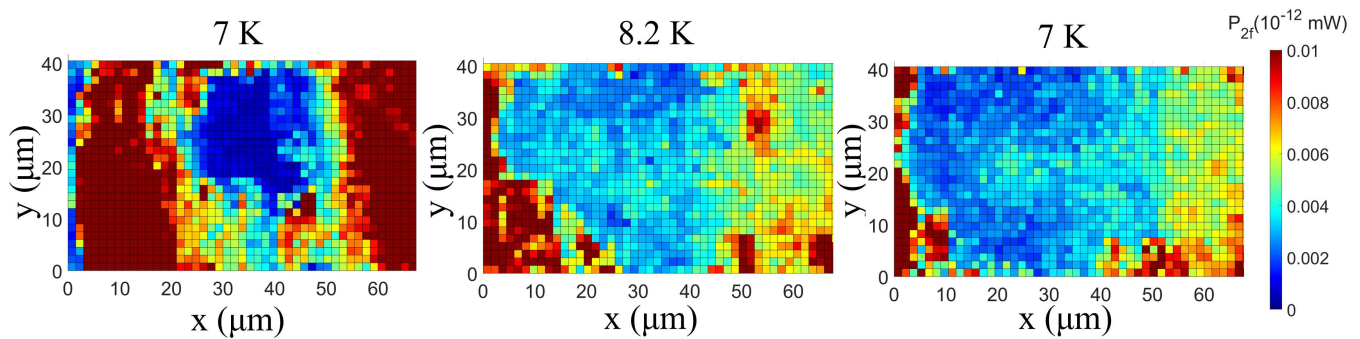


FIG. 13. Three two-dimensional images of $P_{2f}(x, y)$ measured on the Nb film, plotted with a common color-bar (right). The step size is $1.5 \mu\text{m}$. From left to right, the images are obtained successively at 7 K, 8.2 K, and then back to 7 K. The input frequency is 1.81 GHz, and the input power is 6.8 dBm.

- of superconducting radio frequency cavities,” *Superconductor Science and Technology* **38**, 015015 (2024).
- [16] C. Song, M. P. DeFeo, K. Yu, and B. L. T. Plourde, “Reducing microwave loss in superconducting resonators due to trapped vortices,” *Applied Physics Letters* **95**, 232501 (2009).
- [17] C. Song, T. W. Heitmann, M. P. DeFeo, K. Yu, R. McDermott, M. Neeley, John M. Martinis, and B. L. T. Plourde, “Microwave response of vortices in superconducting thin films of Re and Al,” *Phys. Rev. B* **79**, 174512 (2009).
- [18] Serena Eley, Andreas Glatz, and Roland Willa, “Challenges and transformative opportunities in superconductor vortex physics,” *Journal of Applied Physics* **130**, 050901 (2021).
- [19] I. Nsanzineza and B. L. T. Plourde, “Trapping a single vortex and reducing quasiparticles in a superconducting resonator,” *Phys. Rev. Lett.* **113**, 117002 (2014).
- [20] S. Bermon and T. Gheewala, “Moat-guarded Josephson SQUIDs,” *IEEE Transactions on Magnetics* **19**, 1160–1164 (1983).
- [21] Mark Jeffery, T. Van Duzer, J. R. Kirtley, and M. B. Ketchen, “Magnetic imaging of moat-guarded superconducting electronic circuits,” *Applied Physics Letters* **67**, 1769–1771 (1995).
- [22] K Suzuki, H Kawamura, M Maruyama, T Hato, H Suzuki, S Yorozu, Y Kameda, Y Ishimaru, K Nakayama, H Wakana, S Adachi, Y Tarutani, and K Tanabe, “Investigation of the flux state in single-flux-quantum circuits with moats by scanning SQUID microscope,” *Superconductor Science and Technology* **19**, S316 (2006).
- [23] Yuri Polyakov, Supradeep Narayana, and Vasili K. Semenov, “Flux trapping in superconducting circuits,” *IEEE Transactions on Applied Superconductivity* **17**, 520–525 (2007).
- [24] Supradeep Narayana, Yuri A. Polyakov, and Vasili K. Semenov, “Evaluation of flux trapping in superconducting circuits,” *IEEE Transactions on Applied Superconductivity* **19**, 640–643 (2009).
- [25] Kan Fujiwara, Shuichi Nagasawa, Yoshihito Hashimoto, Mutsuo Hidaka, Nobuyuki Yoshikawa, Masamitsu Tanaka, Hiroyuki Akaike, Akira Fujimaki, Kazuyoshi Takagi, and Naofumi Takagi, “Research on effective moat configuration for Nb multi-layer device structure,” *IEEE Transactions on Applied Superconductivity* **19**, 603–606 (2009).
- [26] Vasili K. Semenov and Mikhail M. Khapaev, “How moats protect superconductor films from flux trapping,” *IEEE Transactions on Applied Superconductivity* **26**, 1300710 (2016).
- [27] Kyle Jackman and Coenrad Johann Fourie, “Flux trapping analysis in superconducting circuits,” *IEEE Transactions on Applied Superconductivity* **27**, 1300105 (2017).
- [28] Uday S. Goteti, Han Cai, Jay C. LeFebvre, Shane A. Cybart, and Robert C. Dynes, “Superconducting disordered neural networks for neuromorphic processing with fluxons,” *Science Advances* **8**, eabn4485 (2022).
- [29] Lieze Schindler, Christopher L. Ayala, Naoki Takeuchi, and Nobuyuki Yoshikawa, “The effect of quantised flux on AQFP circuits for a double-active-layered Niobium fabrication process,” *IEEE Transactions on Applied Superconductivity* **34**, 1100908 (2024).
- [30] W. P. M. R. Pathirana and A. Gurevich, “Effect of random pinning on nonlinear dynamics and dissipation of a vortex driven by a strong microwave current,” *Phys. Rev. B* **103**, 184518 (2021).
- [31] M. Golosovsky, M. Tsindlekht, H. Chayet, and D. Davidov, “Vortex depinning frequency in $\text{YBa}_2\text{Cu}_3\text{O}_{7-x}$ superconducting thin films: Anisotropy and temperature dependence,” *Phys. Rev. B* **50**, 470–477 (1994).
- [32] V. V. Moshchalkov, M. Baert, V. V. Metlushko, E. Rosseel, M. J. Van Bael, K. Temst, Y. Bruynseraede, and R. Jonckheere, “Pinning by an antidot lattice: The problem of the optimum antidot size,” *Phys. Rev. B* **57**, 3615–3622 (1998).
- [33] S. Raedts, A. V. Silhanek, M. J. Van Bael, and V. V. Moshchalkov, “Flux-pinning properties of superconducting films with arrays of blind holes,” *Phys. Rev. B* **70**, 024509 (2004).
- [34] A. V. Silhanek, L. Van Look, R. Jonckheere, B. Y. Zhu, S. Raedts, and V. V. Moshchalkov, “Enhanced vortex pinning by a composite antidot lattice in a superconducting Pb film,” *Phys. Rev. B* **72**, 014507 (2005).
- [35] Pedro-de-Jesús Cuadra-Solís, Antoni Fernández-Martínez, Joan Manel Hernández, Antoni García-Liago, Johan Vanacken, and Victor V. Moshchalkov, “A radio-frequency coil for the microwave characterization of vortex dynamics in thin film superconductors,” *Review of Scientific Instruments* **86**, 064701 (2015).
- [36] O.V. Dobrovolskiy, C. González-Ruano, A. Lara, R. Sachser, V.M. Bevez, V.A. Shklovskij, A.I. Bezugov, R.V. Vovk, M. Huth, and F.G. Aliev, “Moving flux

- quanta cool superconductors by a microwave breath,” *Communications Physics* **3**, 64 (2020).
- [37] Sachiko Nakamura, Kota Katsumi, Hiroataka Terai, and Ryo Shimano, “Nonreciprocal terahertz second-harmonic generation in superconducting NbN under supercurrent injection,” *Phys. Rev. Lett.* **125**, 097004 (2020).
- [38] Andrea Alimenti, Nicola Pompeo, Kostiantyn Torokhtii, Tiziana Spina, René Flükiger, Luigi Muzzi, and Enrico Silva, “Microwave measurements of the high magnetic field vortex motion pinning parameters in Nb₃Sn,” *Superconductor Science and Technology* **34**, 014003 (2020).
- [39] Jonathan I. Gittleman and Bruce Rosenblum, “Radio-Frequency resistance in the mixed state for subcritical currents,” *Phys. Rev. Lett.* **16**, 734–736 (1966).
- [40] Mark W. Coffey and John R. Clem, “Unified theory of effects of vortex pinning and flux creep upon the rf surface impedance of type-II superconductors,” *Phys. Rev. Lett.* **67**, 386–389 (1991).
- [41] M. S. Pambianchi, D. H. Wu, L. Ganapathi, and S. M. Anlage, “DC magnetic field dependence of the surface impedance in superconducting parallel plate transmission line resonators,” *IEEE Transactions on Applied Superconductivity* **3**, 2774–2777 (1993).
- [42] Dong Ho Wu, J. C. Booth, and Steven M. Anlage, “Frequency and field variation of vortex dynamics in YBa₂Cu₃O₇– δ ,” *Phys. Rev. Lett.* **75**, 525–528 (1995).
- [43] M Golosovsky, M Tsindlekht, and D Davidov, “High-frequency vortex dynamics in YBa₂Cu₃O₇,” *Superconductor Science and Technology* **9**, 1 (1996).
- [44] Enrico Silva, Nicola Pompeo, and Oleksandr V. Dobrovolskiy, “Vortices at microwave frequencies,” *Physical Sciences Reviews* **2**, 20178004 (2017).
- [45] Sheng-Chiang Lee, C.P. Vlahacos, B.J. Feenstra, Andrew Schwartz, D.E. Steinhauer, F.C. Wellstood, and Steven M. Anlage, “Magnetic permeability imaging of metals with a scanning near-field microwave microscope,” *Applied Physics Letters* **77**, 4404–4406 (2000).
- [46] Sheng-Chiang Lee and S.M. Anlage, “Study of local nonlinear properties using a near-field microwave microscope,” *IEEE Transactions on Applied Superconductivity* **13**, 3594–3597 (2003).
- [47] Sheng-Chiang Lee and Steven M. Anlage, “Spatially-resolved nonlinearity measurements of YBa₂Cu₃O₇– δ bicrystal grain boundaries,” *Applied physics letters* **82**, 1893–1895 (2003).
- [48] Sheng-Chiang Lee, Mathew Sullivan, Gregory R. Ruchti, Steven M. Anlage, Benjamin S. Palmer, B. Maiorov, and E. Osquiguil, “Doping-dependent nonlinear Meissner effect and spontaneous currents in high-T_c superconductors,” *Physical Review B* **71**, 014507 (2005).
- [49] Sheng-Chiang Lee, Su-Young Lee, and Steven M. Anlage, “Microwave nonlinearities of an isolated long YBa₂Cu₃O₇– δ bicrystal grain boundary,” *Physical Review B* **72**, 024527 (2005).
- [50] Dragos I. Mircea, Hua Xu, and Steven M. Anlage, “Phase-sensitive harmonic measurements of microwave nonlinearities in cuprate thin films,” *Physical Review B* **80**, 144505 (2009).
- [51] Tamin Tai, X. X. Xi, C.G. Zhuang, Dragos I. Mircea, and Steven M. Anlage, “Nonlinear near-field microwave microscope for RF defect localization in superconductors,” *IEEE transactions on applied superconductivity* **21**, 2615–2618 (2011).
- [52] Tamin Tai, Behnood G. Ghamsari, and Steven M. Anlage, “Nanoscale electrodynamic response of Nb superconductors,” *IEEE Transactions on Applied Superconductivity* **23**, 7100104–7100104 (2013).
- [53] Tamin Tai, Behnood G. Ghamsari, Thomas R. Bieler, Teng Tan, X. X. Xi, and Steven M. Anlage, “Near-field microwave magnetic nanoscopy of superconducting radio frequency cavity materials,” *Applied Physics Letters* **104**, 232603 (2014).
- [54] Tamin Tai, B.G. Ghamsari, and Steven M. Anlage, “Modeling the nanoscale linear response of superconducting thin films measured by a scanning probe microwave microscope,” *Journal of Applied Physics* **115**, 203908 (2014).
- [55] Tamin Tai, Behnood G. Ghamsari, Tom Bieler, and Steven M. Anlage, “Nanoscale nonlinear radio frequency properties of bulk Nb: Origins of extrinsic nonlinear effects,” *Physical Review B* **92**, 134513 (2015).
- [56] Bakhrom Oripov, Thomas Bieler, Gianluigi Ciovati, Sergio Calatroni, Pashupati Dhakal, Tobias Junginger, Oleg B. Malyshev, Giovanni Terenziani, Anne-Marie Valente-Feliciano, Reza Valizadeh, *et al.*, “High-frequency nonlinear response of superconducting cavity-grade Nb surfaces,” *Physical Review Applied* **11**, 064030 (2019).
- [57] Chung-Yang Wang, Carlota Pereira, Stewart Leith, Guillaume Rosaz, and Steven M. Anlage, “Microscopic examination of rf-cavity-quality niobium films through local nonlinear microwave response,” *Physical Review Applied* **22**, 054010 (2024).
- [58] Chung-Yang Wang and Steven M. Anlage, “Near-field nonlinear microwave microscope for fundamental superconducting studies,” in *2024 IEEE/MTT-S International Microwave Symposium - IMS 2024* (2024) pp. 998–1001.
- [59] Viacheslav V Dremov, Sergey Yu Grebenchuk, Andrey G Shishkin, Denis S Baranov, Razmik A Hovhannisyann, Olga V Skryabina, Nickolay Lebedev, Igor A Golovchanskiy, Vladimir I Chichkov, Christophe Brun, *et al.*, “Local Josephson vortex generation and manipulation with a magnetic force microscope,” *Nature communications* **10**, 4009 (2019).
- [60] Lior Embon, Yonathan Anahory, Alexander Suhov, Dorri Halbertal, Jo Cuppens, Anton Yakovenko, Aviram Uri, Yuri Myasoedov, Michael L Rappaport, Martin E Huber, *et al.*, “Probing dynamics and pinning of single vortices in superconductors at nanometer scales,” *Scientific reports* **5**, 7598 (2015).
- [61] Logan Bishop-Van Horn, Eli Mueller, and Kathryn A. Moler, “Vortex dynamics induced by scanning SQUID susceptometry,” *Phys. Rev. B* **107**, 224509 (2023).
- [62] Marek Foltyn, Konrad Norowski, Alexander Savin, and Maciej Zgirski, “Quantum thermodynamics with a single superconducting vortex,” *Science Advances* **10**, eado4032 (2024).
- [63] An-Lei Zhang, Cun Xue, and Jun-Yi Ge, “Direct imaging of vortex pinning at artificial antidots with different geometries,” *Applied Physics Letters* **115**, 132601 (2019).
- [64] C. Chen, Y. Liu, Y. Chen, Y. N. Hu, T. Z. Zhang, D. Li, X. Wang, C. X. Wang, Z. Y. W. Lu, Y. H. Zhang, Q. L. Zhang, X. L. Dong, R. Wang, D. L. Feng, and T. Zhang, “Revealing the microscopic mecha-

- nism of elementary vortex pinning in superconductors,” *Phys. Rev. X* **14**, 041039 (2024).
- [65] Carson Jeffries, Q. Harry Lam, Youngtae Kim, L. C. Bourne, and A. Zettl, “Symmetry breaking and nonlinear electrodynamics in the ceramic superconductor YBa₂Cu₃O₇,” *Phys. Rev. B* **37**, 9840–9843 (1988).
- [66] L. Ji, R. H. Sohn, G. C. Spalding, C. J. Lobb, and M. Tinkham, “Critical-state model for harmonic generation in high-temperature superconductors,” *Phys. Rev. B* **40**, 10936–10945 (1989).
- [67] K.-H. Müller, J.C. Macfarlane, and R. Driver, “Nonlinear magnetic flux response in high temperature superconductors,” *Physica C: Superconductivity and its Applications* **158**, 366–370 (1989).
- [68] C. D. Jeffries, Q. H. Lam, Y. Kim, C. M. Kim, A. Zettl, and M. P. Klein, “Nonlinear electrodynamics in the granular superconductor YBa₂Cu₃O₇: Experiments and interpretation,” *Phys. Rev. B* **39**, 11526–11537 (1989).
- [69] T. Ishida and R. B. Goldfarb, “Fundamental and harmonic susceptibilities of YBa₂Cu₃O₇– δ ,” *Phys. Rev. B* **41**, 8937–8948 (1990).
- [70] K. Yamamoto, H. Mazaki, H. Yasuoka, S. Katsuyama, and K. Kosuge, “Harmonic susceptibilities of a sintered oxide superconductor,” *Phys. Rev. B* **46**, 1122–1129 (1992).
- [71] S. Shatz, A. Shaulov, and Y. Yeshurun, “Universal behavior of harmonic susceptibilities in type-II superconductors,” *Phys. Rev. B* **48**, 13871–13880 (1993).
- [72] Alan M Portis, *Electrodynamics of high-temperature superconductors*, Vol. 48 (World Scientific, 1993).
- [73] T B Samoilova, “Non-linear microwave effects in thin superconducting films,” *Superconductor Science and Technology* **8**, 259 (1995).
- [74] Daniel E. Oates, “Nonlinear behavior of superconducting devices,” in *Microwave Superconductivity*, edited by Harold Weinstock and Martin Nisenoff (Springer Netherlands, Dordrecht, 2001) pp. 117–148.
- [75] A V Velichko, M J Lancaster, and A Porch, “Non-linear microwave properties of high T_c thin films,” *Superconductor Science and Technology* **18**, R24 (2005).
- [76] D. E. Oates, S.-H. Park, and G. Koren, “Observation of the nonlinear meissner effect in YBCO thin films: Evidence for a *d*-wave order parameter in the bulk of the cuprate superconductors,” *Phys. Rev. Lett.* **93**, 197001 (2004).
- [77] Alexander P. Zhuravel, B. G. Ghamsari, C. Kurter, P. Jung, S. Remillard, J. Abrahams, A. V. Lukashenko, Alexey V. Ustinov, and Steven M. Anlage, “Imaging the anisotropic nonlinear meissner effect in nodal YBa₂Cu₃O₇– δ thin-film superconductors,” *Phys. Rev. Lett.* **110**, 087002 (2013).
- [78] Bakhrom Oripov and Steven M. Anlage, “Time-dependent Ginzburg-Landau treatment of rf magnetic vortices in superconductors: Vortex semiloops in a spatially nonuniform magnetic field,” *Physical Review E* **101**, 033306 (2020).
- [79] M Tabib-Azar, N S Shoemaker, and S Harris, “Non-destructive characterization of materials by evanescent microwaves,” *Measurement Science and Technology* **4**, 583 (1993).
- [80] C. P. Vlahacos, R. C. Black, S. M. Anlage, A. Amar, and F. C. Wellstood, “Near-field scanning microwave microscope with 100 μ m resolution,” *Applied Physics Letters* **69**, 3272–3274 (1996).
- [81] D. E. Steinhauer, C. P. Vlahacos, S. K. Dutta, F. C. Wellstood, and Steven M. Anlage, “Surface resistance imaging with a scanning near-field microwave microscope,” *Applied Physics Letters* **71**, 1736–1738 (1997).
- [82] D. E. Steinhauer, C. P. Vlahacos, S. K. Dutta, B. J. Feenstra, F. C. Wellstood, and Steven M. Anlage, “Quantitative imaging of sheet resistance with a scanning near-field microwave microscope,” *Applied Physics Letters* **72**, 861–863 (1998).
- [83] C. P. Vlahacos, D. E. Steinhauer, S. K. Dutta, B. J. Feenstra, Steven M. Anlage, and F. C. Wellstood, “Quantitative topographic imaging using near-field scanning microwave microscope,” *Applied Physics Letters* **72**, 1778–1780 (1998).
- [84] M. Tabib-Azar, P. S. Pathak, G. Ponchak, and S. LeClair, “Nondestructive superresolution imaging of defects and nonuniformities in metals, semiconductors, dielectrics, composites, and plants using evanescent microwaves,” *Review of Scientific Instruments* **70**, 2783–2792 (1999).
- [85] S.M. Anlage, D.E. Steinhauer, C.P. Vlahacos, B.J. Feenstra, A.S. Thanawalla, Wensheng Hu, S.K. Dutta, and F.C. Wellstood, “Superconducting material diagnostics using a scanning near-field microwave microscope,” *IEEE Transactions on Applied Superconductivity* **9**, 4127–4132 (1999).
- [86] Steven M. Anlage, D. E. Steinhauer, B. J. Feenstra, C. P. Vlahacos, and F. C. Wellstood, “Near-field microwave microscopy of materials properties,” in *Microwave Superconductivity*, edited by Harold Weinstock and Martin Nisenoff (Springer Netherlands, Dordrecht, 2001) pp. 239–269.
- [87] Björn T. Rosner and Daniel W. van der Weide, “High-frequency near-field microscopy,” *Review of Scientific Instruments* **73**, 2505–2525 (2002).
- [88] Atif Imtiaz and Steven M. Anlage, “A novel STM-assisted microwave microscope with capacitance and loss imaging capability,” *Ultramicroscopy* **94**, 209–216 (2003).
- [89] Alexander Tselev, Steven M. Anlage, Hans M. Christen, Robert L. Moreland, Vladimir V. Talanov, and Andrew R. Schwartz, “Near-field microwave microscope with improved sensitivity and spatial resolution,” *Review of Scientific Instruments* **74**, 3167–3170 (2003).
- [90] Atif Imtiaz, Marc Pollak, Steven M. Anlage, John D. Barry, and John Melngailis, “Near-field microwave microscopy on nanometer length scales,” *Journal of Applied Physics* **97**, 044302 (2005).
- [91] Atif Imtiaz and Steven M. Anlage, “Effect of tip geometry on contrast and spatial resolution of the near-field microwave microscope,” *Journal of Applied Physics* **100**, 044304 (2006).
- [92] S. M. Anlage, V. V. Talanov, and A. R. Schwartz, “Principles of near-field microwave microscopy,” in *Scanning Probe Microscopy: Electrical and Electromechanical Phenomena at the Nanoscale*, Vol. 1, edited by S. V. Kalinin and A. Gruverman (Springer-Verlag, New York, 2007) pp. 215–253.
- [93] Atif Imtiaz, Steven M. Anlage, John D. Barry, and John Melngailis, “Nanometer-scale material contrast imaging with a near-field microwave microscope,” *Applied Physics Letters* **90**, 143106 (2007).
- [94] Alexander Tselev, Steven M. Anlage, Zhengkun Ma, and John Melngailis, “Broadband dielec-

- tric microwave microscopy on micron length scales,” *Review of Scientific Instruments* **78**, 044701 (2007).
- [95] Mark E Barber, Eric Yue Ma, and Zhi-Xun Shen, “Microwave impedance microscopy and its application to quantum materials,” *Nature Reviews Physics* **4**, 61–74 (2022).
- [96] S.M. Anlage, C.P. Vlahacos, S. Dutta, and F.C. Wellstood, “Scanning microwave microscopy of active superconducting microwave devices,” *IEEE Transactions on Applied Superconductivity* **7**, 3686–3689 (1997).
- [97] Ashfaq S. Thanawalla, S. K. Dutta, C. P. Vlahacos, D. E. Steinhauer, B. J. Feenstra, Steven M. Anlage, F. C. Wellstood, and Robert B. Hammond, “Microwave near-field imaging of electric fields in a superconducting microstrip resonator,” *Applied Physics Letters* **73**, 2491–2493 (1998).
- [98] Wensheng Hu, A. S. Thanawalla, B. J. Feenstra, F. C. Wellstood, and Steven M. Anlage, “Imaging of microwave intermodulation fields in a superconducting microstrip resonator,” *Applied Physics Letters* **75**, 2824–2826 (1999).
- [99] Steven M. Anlage, “Microwave superconductivity,” *IEEE Journal of Microwaves* **1**, 389–402 (2021).
- [100] Yusuke Kato, “Charging effect on the Hall conductivity of single vortex in type II superconductors,” *Journal of the Physical Society of Japan* **68**, 3798–3801 (1999).
- [101] Jennifer Deang, Qiang Du, and Max D. Gunzburger, “Stochastic dynamics of Ginzburg-Landau vortices in superconductors,” *Phys. Rev. B* **64**, 052506 (2001).
- [102] Jennifer Deang, Qiang Du, and Max D. Gunzburger, “Modeling and computation of random thermal fluctuations and material defects in the Ginzburg-Landau model for superconductivity,” *Journal of Computational Physics* **181**, 45–67 (2002).
- [103] Alexander D. Hernández and Daniel Domínguez, “Dissipation spots generated by vortex nucleation points in mesoscopic superconductors driven by microwave magnetic fields,” *Physical Review B* **77**, 224505 (2008).
- [104] Antonio Lara, Farkhad G. Aliev, Alejandro V. Silhanek, and Victor V. Moshchalkov, “Microwave-stimulated superconductivity due to presence of vortices,” *Scientific reports* **5**, 9187 (2015).
- [105] Alden R. Pack, Jared Carlson, Spencer Wadsworth, and Mark K. Transtrum, “Vortex nucleation in superconductors within time-dependent Ginzburg-Landau theory in two and three dimensions: role of surface defects and material inhomogeneities,” *Physical Review B* **101**, 144504 (2020).
- [106] Qing-Yu Wang, Cun Xue, Chao Dong, and You-He Zhou, “Effects of defects and surface roughness on the vortex penetration and vortex dynamics in superconductor-insulator-superconductor multilayer structures exposed to RF magnetic fields: numerical simulations within TDGL theory,” *Superconductor Science and Technology* **35**, 045004 (2022).
- [107] Igor Bogush, Oleksandr V. Dobrovolskiy, and Vladimir M. Fomin, “Microwave generation and vortex jets in superconductor nanotubes,” *Phys. Rev. B* **109**, 104516 (2024).
- [108] Ryohei Wakatsuki, Yu Saito, Shintaro Hoshino, Yuki M. Itahashi, Toshiya Ideue, Motohiko Ezawa, Yoshihiro Iwasa, and Naoto Nagaosa, “Nonreciprocal charge transport in noncentrosymmetric superconductors,” *Science Advances* **3**, e1602390 (2017).
- [109] Yuki M. Itahashi, Yu Saito, Toshiya Ideue, Tsutomu Nojima, and Yoshihiro Iwasa, “Quantum and classical ratchet motions of vortices in a two-dimensional trigonal superconductor,” *Phys. Rev. Res.* **2**, 023127 (2020).
- [110] C-S Lee, Boldizsar Janko, Imre Derenyi, and A-L Barabási, “Reducing vortex density in superconductors using the ‘ratchet effect’,” *Nature* **400**, 337–340 (1999).
- [111] Clécio C. de Souza Silva, J. Van de Vondel, B. Y. Zhu, M. Morelle, and V. V. Moshchalkov, “Vortex jet effects in films with a periodic array of antidots,” *Phys. Rev. B* **73**, 014507 (2006).
- [112] Britton LT Plourde, “Nanostructured superconductors with asymmetric pinning potentials: Vortex ratchets,” *IEEE transactions on applied superconductivity* **19**, 3698–3714 (2009).
- [113] B. B. Jin, B. Y. Zhu, R. Wördenweber, C. C. de Souza Silva, P. H. Wu, and V. V. Moshchalkov, “High-frequency vortex ratchet effect in a superconducting film with a nanoengineered array of asymmetric pinning sites,” *Phys. Rev. B* **81**, 174505 (2010).
- [114] G. R. Berdiyrov, M. V. Milošević, and F. M. Peeters, “Novel commensurability effects in superconducting films with antidot arrays,” *Phys. Rev. Lett.* **96**, 207001 (2006).
- [115] G. R. Berdiyrov, M. V. Milošević, and F. M. Peeters, “Superconducting film with weak pinning centers: Incommensurate vortex lattices,” *Phys. Rev. B* **76**, 134508 (2007).
- [116] S. C. Sanders, J. Sok, D. K. Finnemore, and Qiang Li, “Thermally activated hopping of a single Abrikosov vortex,” *Phys. Rev. B* **47**, 8996–9000 (1993).
- [117] M. R. Beasley, R. Labusch, and W. W. Webb, “Flux creep in type-II superconductors,” *Phys. Rev.* **181**, 682–700 (1969).
- [118] Junghyun Sok and D. K. Finnemore, “Thermal depinning of a single superconducting vortex in Nb,” *Phys. Rev. B* **50**, 12770–12773 (1994).
- [119] J. Gail, M. Mück, and C. Heiden, “Pinning and depinning of single vortices in niobium thin film dc superconducting quantum interference devices,” *Applied Physics Letters* **73**, 2663–2665 (1998).
- [120] Y. Yeshurun and A. P. Malozemoff, “Giant flux creep and irreversibility in an Y-Ba-Cu-O crystal: An alternative to the superconducting-glass model,” *Phys. Rev. Lett.* **60**, 2202–2205 (1988).
- [121] M. Tinkham, “Resistive transition of high-temperature superconductors,” *Phys. Rev. Lett.* **61**, 1658–1661 (1988).
- [122] J. I. Martín, M. Vélez, A. Hoffmann, Ivan K. Schuller, and J. L. Vicent, “Temperature dependence and mechanisms of vortex pinning by periodic arrays of Ni dots in Nb films,” *Phys. Rev. B* **62**, 9110–9116 (2000).
- [123] Y. Z. Zhang, H. H. Wen, and Z. Wang, “Thermally activated energies of $\text{YBa}_2\text{Cu}_3\text{O}_{7-\delta}$ and $\text{Y}_0.8\text{Ca}_{0.2}\text{Ba}_2\text{Cu}_3\text{O}_{7-\delta}$ thin films,” *Phys. Rev. B* **74**, 144521 (2006).
- [124] Y Z Zhang, Z A Ren, and Z X Zhao, “Thermally activated energy and critical magnetic fields of $\text{SmFeAsO}_{0.9}\text{F}_{0.1}$,” *Superconductor Science and Technology* **22**, 065012 (2009).
- [125] WJ Choi, YI Seo, D Ahmad, and Yong Seung Kwon, “Thermal activation energy of 3D vortex matter in $\text{NaFe}_{1-x}\text{Co}_x\text{As}$ ($x=0.01, 0.03$ and 0.07) single crystals,” *Scientific Reports* **7**, 10900 (2017).
- [126] Sameh M. Altanany, I. Zajcewa, T. Zajarniuk,

- A. Szewczyk, and Marta Z. Cieplak, “Vortex dynamics in disordered niobium thin films,” *Phys. Rev. B* **109**, 214504 (2024).
- [127] Michael Tinkham, *Introduction to superconductivity* (Dover Publications, Mineola, NY, 2004).
- [128] Armen Gulian, *Shortcut to superconductivity* (Springer Nature, Switzerland, 2020).